ARTICLE

Transparent Infrared-Emitting CeF_3:Yb−Er Polymer Nanocomposites for Optical Applications

Mei Chee Tan, Swanand D. Patil, and Richard E. Riman*

Department of Materials Science and Engineering, Rutgers, The State University of New Jersey, 607 Taylor Road, Piscataway, New Jersey 08854

ABSTRACT Bright infrared-emitting nanocomposites of unmodified CeF_3:Yb−Er with polymethyl-methacrylate (PMMA) and polystyrene (PS), which offer a vast range of potential applications, which include optical amplifiers, waveguides, laser materials, and implantable medical devices, were developed. For the optical application of these nanocomposites, it is critical to obtain highly transparent composites to minimize absorption and scattering losses. Preparation of transparent composites typically requires powder processing approaches that include sophisticated particle size control, deagglomeration, and dispersion stabilization methods leading to an increase in process complexity and processing steps. This work seeks to prepare transparent composites with high solids loading (>5 vol %) by matching the refractive index of the inorganic particle with low cost polymers like PMMA and PS, so as to circumvent the use of any complex processing techniques or particle surface modification. PS nanocomposites were found to exhibit better transparency than the PMMA nanocomposites, especially at high solids loading (≥10 vol %). It was found that the optical transparency of PMMA nanocomposites was more significantly affected by the increase in solids loading and inorganic particle size because of the larger refractive index mismatch of the PMMA nanocomposites compared to that of PS nanocomposites. Rayleigh scattering theory was used to provide a theoretical estimate of the scattering losses in these ceramic-polymer nanocomposites.

KEYWORDS: infrared-emitting • phosphors • polymer composites • transparent

1. INTRODUCTION

Erbium-doped infrared-emitting materials have been extensively used in integrated optical devices like fiber amplifiers and waveguides for telecommunications (1, 2). The high processing costs of inorganic ceramic waveguides fabricated using physical methods like melt processing, molecular beam epitaxy, ion implantation, or laser deposition (3−9), have driven the development of low-cost, tunable polymer waveguide materials (10−15). However, the performance of polymer waveguides is limited by the low solubility of rare earth ions and the emission-quenching organic functional groups (e.g., −OH, −CH) commonly found in polymers. Rare earth clusters improve rare-earth ion solubility while preventing quenching of emissions from polymer functional groups (14). Because these rare earth clusters suffer from poor chemical and thermal stability, materials processing conditions in a controlled atmosphere consisting of low oxygen and water concentrations are required. These limitations have motivated the development of inorganic nanoparticle−polymer waveguide composites (16−18). These nanocomposites combine the advantages of organic polymers (lightweight, flexibility, good impact resistance, and excellent processability) and inorganic host materials (low phonon energy, intense emissions, chemical durability and high thermal stability).

High optical transparency and high inorganic solids loading with high absorption and emission cross-sections are desired for highly emissive nanocomposites. One of the methods of preparing transparent composites is to have an excellent dispersion of small particles (<100 nm). Achieving this requires particle processing approaches that include sophisticated size control, deagglomeration, and dispersion stabilization methods leading to an increase in process complexity and processing steps (19−23). Transparent composites with low solids loading (<3 vol %) using surface modified nanophosphors (16, 23−26), and high solids loading (~80 wt %) using costly polymers and processing methods (22) have been reported elsewhere. This work seeks to prepare transparent composites with high solids loading (>5 vol %) by matching the refractive index of the inorganic particle with low cost polymers like polymethyl-methacrylate (PMMA) and polystyrene (PS), so as to circumvent the use of any complex processing techniques or particle surface modification. This will enable the determination of whether control of the refractive index alone can be sufficient for making transparent nanocomposites without using any aggressive particle deagglomeration techniques or surface modification of the nanoparticles.

To obtain highly transparent composites, it is critical to minimize absorption and scattering losses. Theoretical transmittance (T) of nanocomposites where absorption losses dominate can be determined using the Beer−Lambert law as shown in eq 1 (27).

* Corresponding author. Email: riman@rci.rutgers.edu.
Received for review March 16, 2010 and accepted May 28, 2010
DOI: 10.1021/am100228j

Published on Web 06/09/2010

$$T = \frac{I}{I_o} = \exp(-\varepsilon x c) \quad (1)$$

where I is transmitted intensity, I_o is incident intensity, x is optical path length, c is concentration of absorbing species, and ε is molar extinction coefficient, which is a material property and a function of the wavelength of incident light.

In the case where scattering losses dominate, theoretical transmittance of nanocomposites can be estimated using Rayleigh scattering theory as a guide (16, 19−27)

$$T = \frac{I}{I_o} = \exp\left\{-\frac{32\pi^4 \phi_p x r^3 n_m^4}{\lambda^4}\left[\frac{(n_p/n_m)^2 - 1}{(n_p/n_m)^2 + 2}\right]^2\right\} \quad (2)$$

where λ is wavelength of incident light, ϕ_p is volume fraction of inorganic particles, r is size of inorganic particle, n_p is refractive index of inorganic particle and n_m is refractive index of polymer matrix. The assumptions and inadequacies of the Rayleigh scattering model will be addressed later. Refractive index, n_i is an intrinsic material property that is dependent on λ (see eq 3), where C_j for $j = 0-5$ are material dependent constants (28). The Cauchy formalism for refractive index in eq 3 was used in this work due to the lack of available information on the Sellmeier coefficients for PMMA and PS. The Sellmeier formalism for refractive index is often preferred because it provides physical meaning to the fitting parameters.

$$n_i^2 = C_o + C_1\lambda^2 + C_2\lambda^{-2} + C_3\lambda^{-4} + C_4\lambda^{-6} + C_5\lambda^{-8} \quad (3)$$

Equation 2 shows that the inorganic particle size, solids loading and refractive index mismatch, Δn between the inorganic phase and polymer matrix are factors that affect the transparency of nanocomposites. The inorganic particle size is controlled by the primary particle size and agglomerate or aggregate size (secondary particle size) (29). The primary particle size is determined by the processing methods (e.g., synthesis and heat treatment conditions) used to prepare the particles. The secondary particle size is governed by the surface characteristics of nanoparticles, which influence the quality of particle dispersion in the polymer matrix.

Both eqs 1 and 2 can be expressed as $\ln T = A\lambda^b$. When absorption losses dominate as shown in eq 1, A varies linearly with c and x, where c has a linear relationship with solids loading. The value of A also depends on the absorption efficiency of the absorbing species. The value of b is governed mainly by the material dependent relationship of ε with λ. The inclusion of scattering effects to absorption losses on transmittance will lead to changes in the b value. A also varies linearly with solids loading in the case where Rayleigh scattering losses dominate, because $A\tilde{F}\phi_p x r^3$ and F is a constant. The value of b is approximately -4. However, considering the relationship of n_i with λ as shown in eq 3, deviations from -4 are expected.

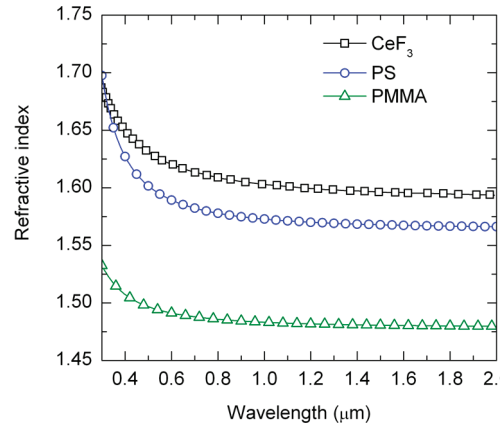

FIGURE 1. Refractive index of PMMA, PS, and CeF_3 (20, 21).

CeF_3:Yb−Er nanoparticles were found to display an intense infrared emission at ~1530 nm, where undesired parasitic emissions are avoided by using an active host which interacts and enhances energy transfer to the rare earth luminescent center (30). In this work, transparent composites with high solids loading were obtained by mixing nonsurface modified CeF_3:Yb−Er nanoparticles with a polymer that has a small index mismatch with CeF_3. This study will evaluate the effects of a large and small refractive index mismatch by comparing the difference in transparency obtained using CeF_3 and PS ($\Delta n \approx 0.03$), and CeF_3 and PMMA ($\Delta n \approx 0.12$) (see Figure 1) (28, 31). The effects of solids loading and inorganic particle size on the transparency of CeF_3:Yb−Er nanocomposites are also discussed in this paper.

2. EXPERIMENTAL METHODS

2.1. Synthesis of CeF_3:Yb−Er Nanoparticles (30). Stoichiometric amounts of 99.5% cerium(III) nitrate, 99.9% erbium(III) nitrate, 99.9% ytterbium(III) nitrate, and 98% ammonium fluoride (Sigma Aldrich, St. Louis, MI) were mixed in ~75 mL of water for 30 min. This mixture was then transferred to a 125 mL Teflon liner and heated to ~200 °C for 2 h in a Parr pressure vessel (Parr Instrument Company, Moline, IL). The as-synthesized nanoparticles were washed three times in deionized water by centrifuging (Beckman-Coulter Avanti J-26 XP, Fullerton, CA) and dried at 70 °C in air in a mechanical convection oven (Thermo Scientific Thermolyne, Waltham, MA) for further powder characterization. CeF_3:Yb−Er nanoparticles with particle sizes of ~14 ± 6 nm were synthesized. Heat-treatment of as-synthesized particles was completed in a controlled environment using the double crucible method to prevent CeF_3 oxidation. Ten and 50 mL alumina crucibles (CoorsTek, Golden, CO) were used for the heat-treatment. ~0.9 g of as-synthesized nanoparticles were placed in the inner 10 mL crucible. The outer 50 mL crucible contained ~3.0 g of 95% ammonium bifluoride (Sigma Aldrich). The double crucible assembly was heated at ~400 °C for 1 h in a box furnace (Thermo Scientific Thermolyne, Waltham, MA). After heat treatment, the particle size distribution increased to ~42 ± 15 nm as a result of particle aggregation.

2.2. Preparation of CeF_3:Yb−Er Polymer Nanocomposites.
2.2.1. Polymethyl Methacrylate (PMMA) Nanocomposites. PMMA (molecular weight 35K) and 99% chloroform were purchased from Sigma Aldrich. About 0.08−0.88 g of CeF_3:

Yb−Er were mixed and sonicated in 0.61−1.42 g PMMA in ~5 mL of chloroform. The different mixtures were subsequently poured into 42 mL aluminum dishes (Fisher, Pittsburgh, PA). These mixtures were dried under room temperature conditions for ~3 days to allow the solvent to vaporize. Further solvent removal was completed in vacuo in a vacuum oven (VWR 1410, West Chester, PA) at room temperature.

2.2.2. *Polystyrene (PS) Nanocomposites.* PS (molecular weight 35K) and 98% toluene were purchased from Sigma Aldrich. About 0.07−0.85 g of CeF_3:Yb−Er were mixed and sonicated in 0.65−1.43 g PS in ~5 mL of toluene. The different mixtures were subsequently poured into 42 mL aluminum dishes. These mixtures were dried under room temperature conditions for ~3 days to allow the solvent to vaporize. Further solvent removal was completed in vacuo in a vacuum oven at room temperature.

2.3. Characterization. Samples of the different composites were embedded in low viscosity "Spurr" epoxy (Electron Microscopy Sciences, Hatfield, PA) for transmission electron microscopy (TEM). Vinylcyclophene dioxide (ERL 4221), diglycidyl ether (DER 736), nonenyl succinic anhydride (NSA) and dimethylaminoethanol (DMAE) were mixed in a plastic beaker before the solution was transferred into the embedding mold. Next, sections of the composites were introduced into the resin mixture. Thin sections obtained by sectioning with a glass knife and a LKB ultramicrotome (LKB Instruments, Inc., Rockville, MD), were mounted on grids for imaging. TEM images of samples were taken using the JEOL 100CX transmission electron microscope (JEOL, Tokyo, Japan) equipped with a LaB_6 gun operating at an accelerating voltage of 80 kV.

Difficulties were encountered in obtaining thin sections of PS composite samples during ultramicrotome sectioning primarily due to the brittle nature of PS. Consequently, the cross sections of PS composites were observed using scanning electron microscopy (SEM). SEM images of the PS composite samples were taken using the Carl Zeiss Σigma field-emission scanning electron microscope (Carl Zeiss, Carl Zeiss SMT Inc., Peabody, MA) using a secondary electron detector and operating at an accelerating voltage of 1.0 kV with working distance of 5.0 mm.

The transmittance spectra of nanocomposites from 400 to 700 nm were measured with a 4 nm slit and 1 nm step size, using a Perkin-Elmer Lambda 9 spectrophotometer (Perkin-Elmer, Waltham, MA) that was equipped with a 60 mm integrating sphere. The emission spectra of nanocomposites, excited at ~976 nm with a 0.7 W laser (BW976, BW Tek, Newark, NJ), were collected, focused, and dispersed using a 0.55 m Triax 550 monochromator (Jobin Yvon, Edison, NJ). The signals were detected with a thermoelectrically cooled $In_xGa_{1-x}As$ detector (Electro-Optical Systems, Phoenixville, PA). A lock-in amplifier (SR850 DSP, Stanford Research System, Sunnyvale, CA) amplified the output signal from the detector. The spectrometer and detection systems were interfaced using a data acquisition system that was controlled with Synerjy commercial software (Jobin Yvon, Edison, NJ).

3. RESULTS AND DISCUSSION

Transparent composites with high solids loading were prepared using unmodified CeF_3:Yb−Er nanoparticles and PMMA and PS. Figures 2 and 3 show TEM and SEM micrographs of PMMA and PS nanocomposites, respectively, with different solids loading where interparticle distance decreased with increasing solids loading. A comparison of the particle−polymer interactions between PMMA and PS composites from TEM and SEM images cannot be made since the sampling statistics, penetration depth, and resolution from using the different microscopy techniques are different. However, it can be observed that for both PMMA and PS composites, at solids loading ≤5 vol%, several ~1−2 μm agglomerates were observed. Several other smaller submicrometer sized clusters of 2−5 particles were also observed. At higher solids loading (≥10 vol %), larger agglomerates up to tens of micrometers were observed and most of the

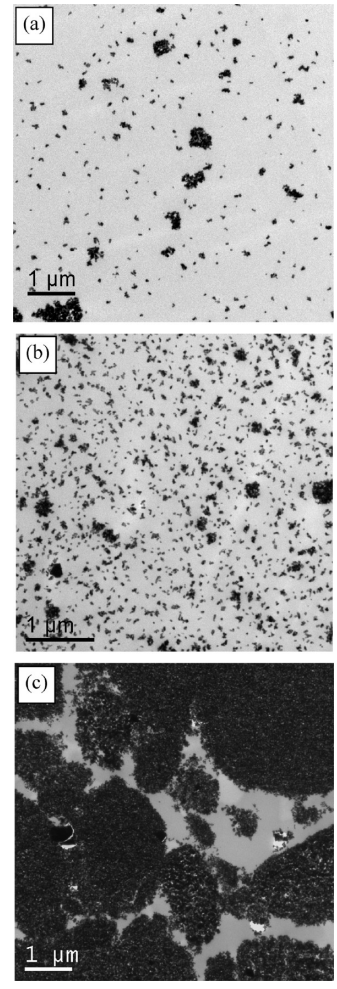

FIGURE 2. TEM micrographs of CeF_3:Yb−Er nanoparticles in PMMA with solids loading of (a) 2, (b) 5, and (c) 10 vol %.

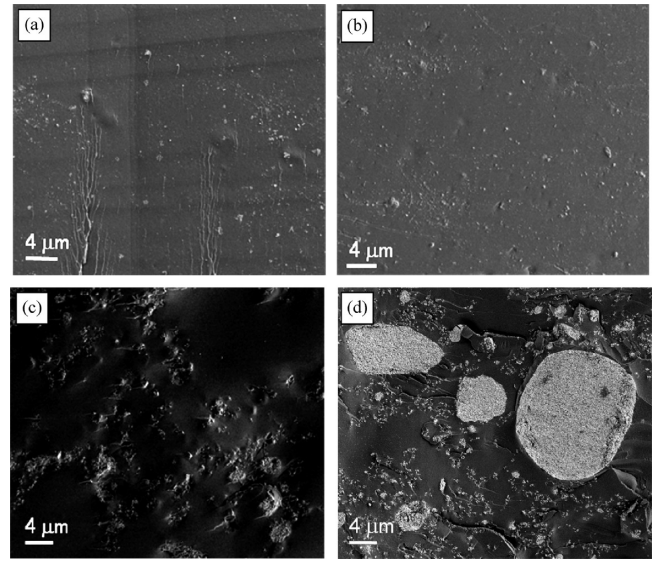

FIGURE 3. SEM micrographs of CeF_3:Yb−Er nanoparticles in PS with solids loading of (a) 1, (b) 2, (c) 5, and (d)10 vol %.

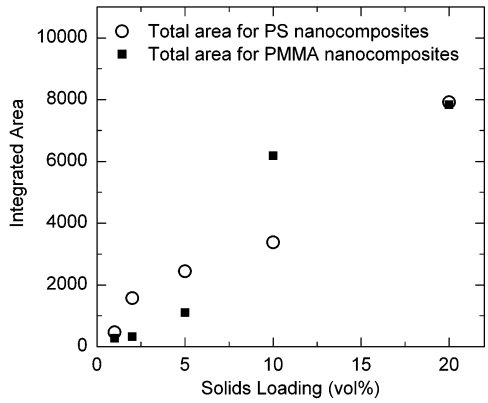

FIGURE 4. Relationship between integrated emission intensity and solids loading for PMMA and PS nanocomposites.

particles were observed to be in contact with one another. The poor dispersion of CeF_3:Yb−Er nanoparticles was attributed to the absence of particle stabilizing forces (e.g., electrostatic repulsion or steric stabilization forces). More effective methods of deagglomeration (e.g., homogenization) were not used because they often introduce undesirable defects such as bubbles in both the polymer−solvent mixture and final polymer composite that are difficult to remove due to the viscous nature of the mixture. Upon excitation at 975 nm, both the PMMA and PS nanocomposites showed an emission at ~1530 nm without any visible upconversion (see the Supporting Information, Figure S-1). This observed emission at ~1530 nm was identical to that from the CeF_3:Yb−Er nanoparticles (30). The integrated emission intensity was found to increase linearly with increasing solids loading for both PMMA and PS nanocomposites (Figure 4).

Accurate prediction of the composites' transmittance at high solids loading based on light scattering theories (e.g., Rayleigh, Debye, Mie, Fraunhoffer) is difficult. The Rayleigh scattering model is applicable only for dilute systems (e.g., upper limit is ~2 vol % for $\lambda = 400$ nm, $r = 20$ nm, and $\Delta n = 0.14$) and it is assumed that the scattering centers are isotropic and nonabsorbing with dimensions no larger than $\lambda/20$ (27). Therefore, the Rayleigh approximation was applicable only for a narrow range of values for λ, n_i, and ϕ_p. Though there are other light scattering models (e.g., Debye, Mie, Fraunhoffer), each of these models often introduces either other constraints and/or increases the level of complexity (27). For instance, for the Debye scattering model, while the limitations on particle size are relaxed, a more stringent constraint is that the system must have a low refractive index such that $(2\pi L_{ch})/(\lambda)(n_i - 1) << 1$, where L_{ch} is characteristic length. Correction factors that account for absorption efficiency, interference effects, particle morphology, and interparticle and intraparticle scattering can be introduced to improve the accuracy of the models while relaxing the constraints on particle sizes and refractive index. However, the level of complexity in the model to take on a full range of values will increase significantly. In this work, theoretical transmittance of nanocomposites is estimated using the Rayleigh scattering theory as a guide to understanding the effects of particle size, refractive index, and solids loading.

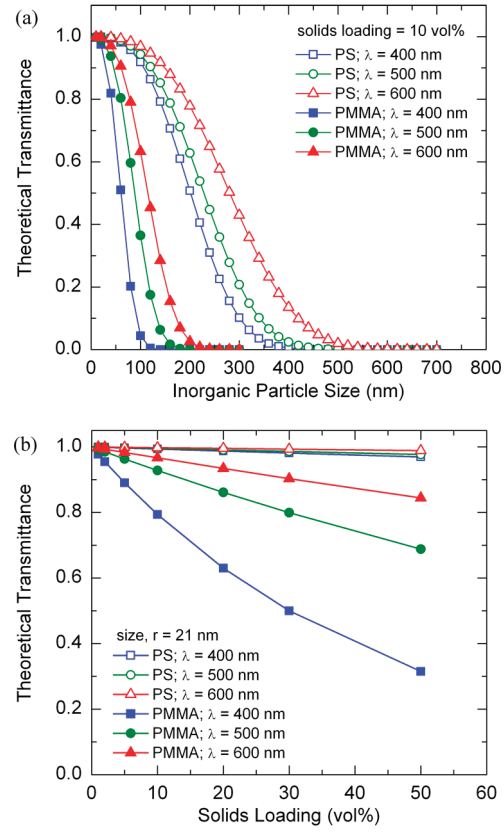

FIGURE 5. Theoretical transmittance for PMMA and PS nanocomposites at incident wavelengths of 400, 500, and 600 nm for different (a) inorganic particle sizes and (b) solids loading.

Theoretical transmittance of the polymer nanocomposites were estimated using eq 2 as shown in Figure 5, using the values of refractive index in Figure 1 and assuming that the optical path length was equivalent to the sample thickness of ~0.1 mm. By reducing index mismatch, the maximum allowable inorganic particle size to achieve the same transparency was increased (Figure 5a). For example, to maintain transmittance of 0.90 at 400 nm, the maximum acceptable allowable particle size was ~30 nm for PMMA nanocomposites compared to ~150 nm for PS nanocomposites. Alternatively, transparency of nanocomposites can be improved by decreasing solids loading (Figure 5b). Transparency of the PMMA nanocomposites is found to be more sensitive to the solids loading because of the larger refractive index mismatch. Photographs of the PMMA and PS nanocomposites with different solids loadings are shown in Figure 6. From this figure, PS nanocomposites exhibit better transparency than PMMA nanocomposites, especially at high solids loading (≥10 vol %). The transparency of PMMA nanocomposites was also more significantly affected by the increased solids loading than the PS nanocomposites. Although low solids loadings were favorable for increased transmittance, an undesired resulting trade-off is weaker emission intensities from the more dilute phosphor solids loading as discussed earlier.

Transmittance measurements for the PMMA and PS nanocomposites at 400, 500, and 600 nm with different solids loading are shown in Figure 7. The transmittance spectra from 400 to 700 nm with different solids loadings

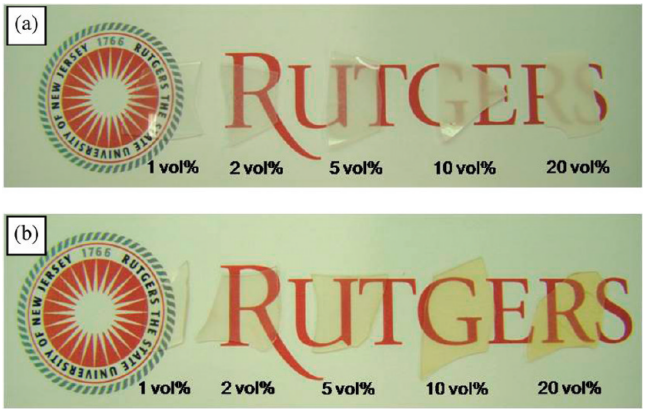

FIGURE 6. (a) PMMA and (b) PS nanocomposites with solids loadings from 1 to 20 vol %.

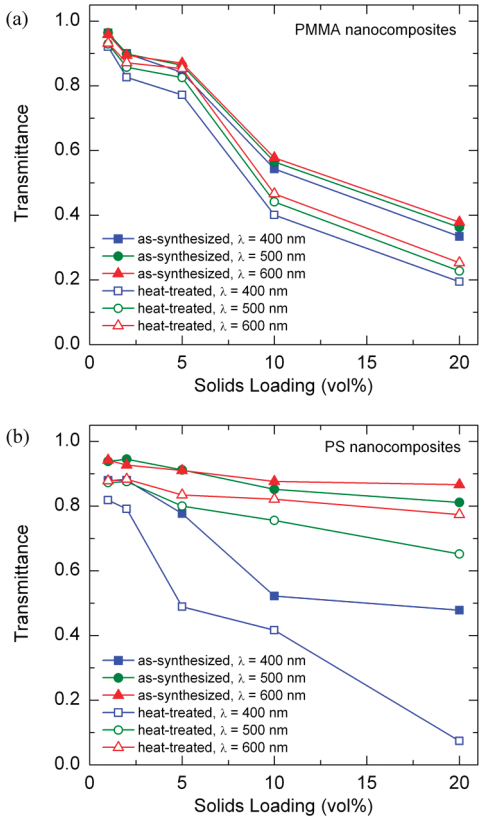

FIGURE 7. Measured transmittance for (a) PMMA and (b) PS nanocomposites at incident wavelengths of 400, 500, and 600 nm for as-synthesized (~14 ± 6 nm) and heat-treated (~42 ± 15 nm) CeF_3:Yb−Er nanoparticles at different solids loadings.

can be found in the Supporting Information (Figure S-2). It was found that PMMA and PS nanocomposites prepared using as-synthesized CeF_3:Yb−Er nanoparticles had higher transmittance compared to that prepared using heat-treated CeF_3:Yb−Er nanoparticles. One possible explanation for the difference in transparencies obtained using as-synthesized and heat-treated CeF_3:Yb−Er nanoparticles is the difference in particle sizes of ~14 ± 6 nm and ~42 ± 15 nm, respectively (30). Composites having a good dispersion of particles are required to determine the actual scattering contribution of particle size on transmittance. Thus, further work utilizing more effective particle dispersion methods is warranted to further quantify the influence of particle size.

From the transmittance data, PS nanocomposites were found to be more transparent than the PMMA nanocomposites, which was consistent with the observations from the photographs in Figure 6. The higher transparency of PS nanocomposites can be attributed to the reduced scattering due to the smaller index mismatch between CeF_3 and PS ($\Delta n \approx 0.03$) than that between CeF_3 and PMMA ($\Delta n \approx 0.12$) as shown in Figure 1.

The relationship between transmittance and wavelength was studied further by comparing the computed theoretical transmittance and the measured transmittance (Figure 7, Figure S-2). The theoretical transmittance at low and high solids loading of 1 and 10 vol% were calculated using equations 2 and 3, assuming that Rayleigh scattering was dominant as shown in Figure 5. Both the theoretically calculated and measured transmittance values were then fitted to the general expression of $\ln T = A\lambda^b$ to extract parameters A and b, as shown in Figures 8 and 9, respectively. As an example, comparing theoretical $A = -1.21 \times 10^{10}$ and $b = -4.51$ with the measured $A = -0.754$ and $b = -0.375$ for PMMA with 1 vol % solids, the measured and theoretical values of A and b as shown in Table 1 were a poor fit. The poor fit between measured and theoretical values for parameters A and b can be attributed to the inherent inadequacies of the Rayleigh scattering model and lack of consideration for the contribution of absorption losses and multiple scattering effects.

From Figure 8 and Table 1, it was found that theoretically when Rayleigh scattering losses were assumed to dominate, b was −4.51 and −2.96 for PMMA and PS composites, respectively. It was also shown that the constant A increased by 10 times when solids loading was increased by 10 times for both PMMA and PS composites. Large differences were found between the fitted experimental values of b for PMMA composites with solids loading of 1 and 10 vol% and that of the theoretical values determined by assuming that Rayleigh scattering dominated (see Table 1). For the PS composites with solids loading of 1 and 10 vol %, $\ln T$ was found to relate differently with λ in the regions of 400−460 nm and 470−700 nm (see Table 1). The regions were fitted separated to evaluate the $(\ln T)-\lambda$ relations and determine parameters A_1 and b_1 and A_2 and b_2 for regions 1 (470−700 nm) and 2 (400−460 nm), respectively. The occurrence of different $(\ln T)-\lambda$ relations in separate λ regions suggests that there was more than one mechanism governing optical losses, where the contribution of each loss mechanism was also a function of λ. The fitted experimental values of b for PS composites were observed to be mostly different from the theoretical values obtained by assuming that Rayleigh scattering dominated (see Table 1). However, for the PS composites with 1 vol % solids loading in the region of 400−460 nm, b was found to closely match the theoretically estimated value of −2.96 for PS composites. This suggests that scattering losses most likely dominated in the region of 400−460 nm for PS composites at 1 vol %. Negative peaks (i.e., absorption peaks) characteristic of Er-doped materials at 486, 519, and 650 nm (32) were also observed for both

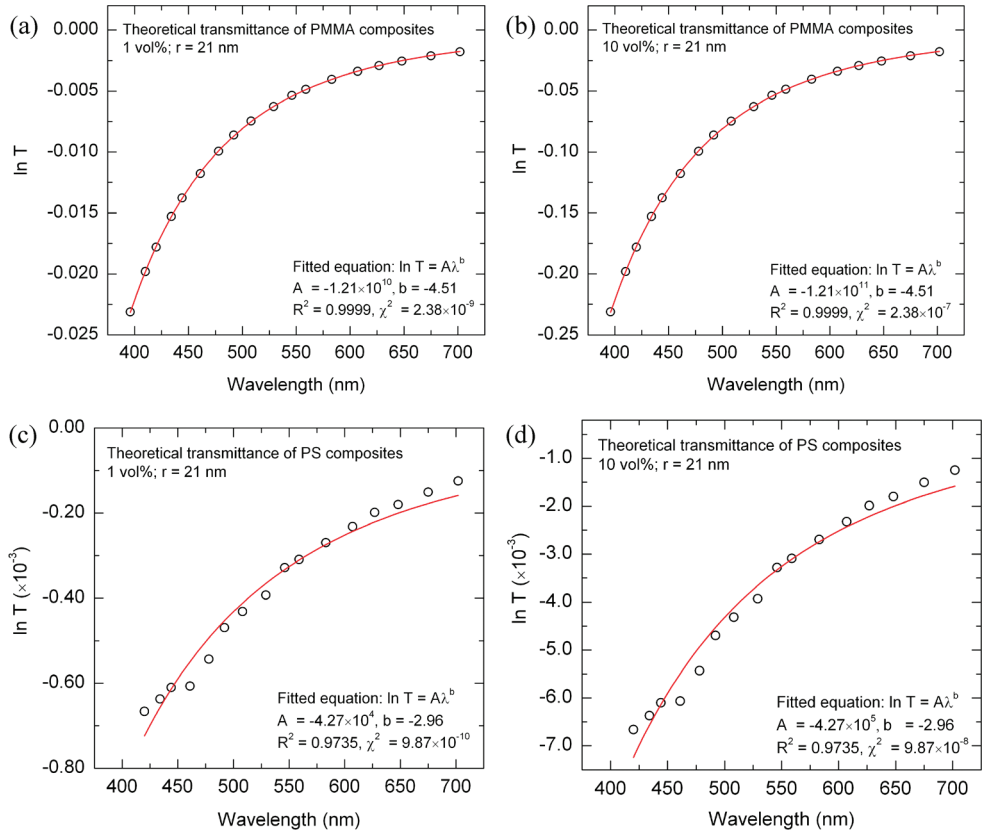

FIGURE 8. Relationship of ln T with λ at different solids loading for PMMA at (a) 1 and (b) 10 vol %, and PS at (c) 1 and (d) 10 vol %, where T was the theoretical transmittance calculated assuming Rayleigh scattering losses dominated.

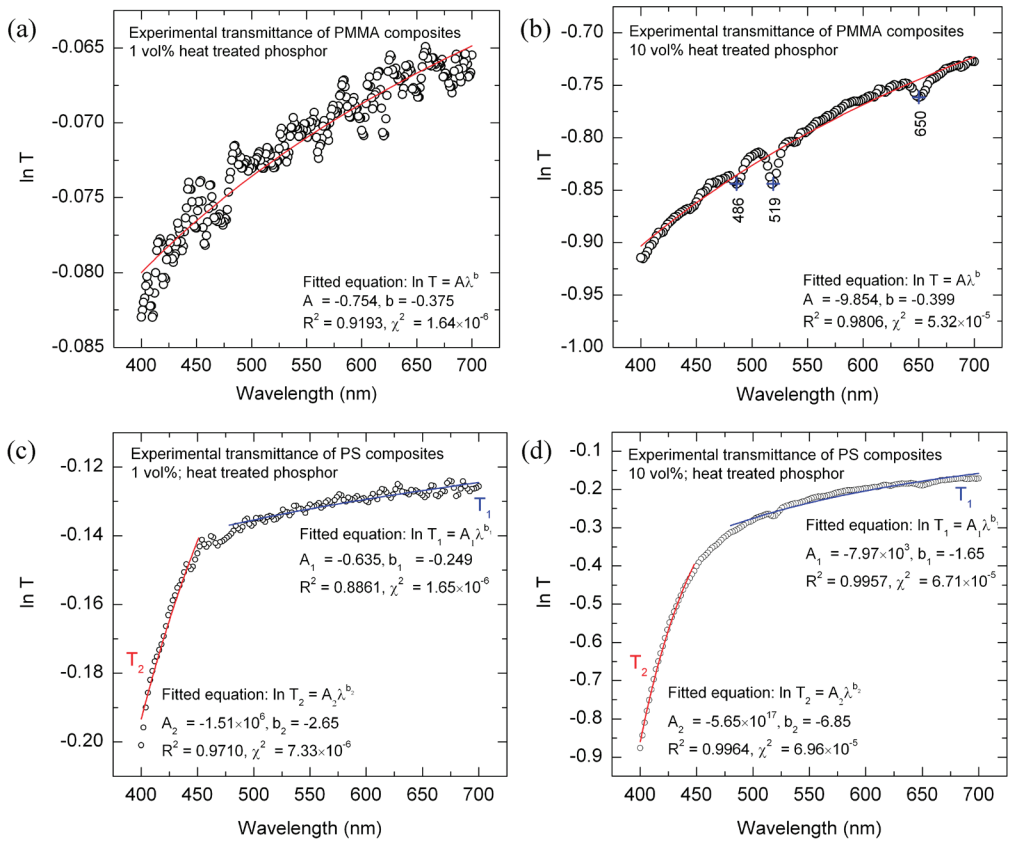

FIGURE 9. Relationship of ln T with λ at different solids loading for PMMA at (a) 1 and (b) 10 vol %, and PS at (c) 1 and (d) 10 vol %, where T was the measured transmittance.

Table 1. Fitted Values of Parameters *A* and *b* for Theoretical and Measured Transmittance

	theoretical		measured	
	A	*b*	*A*	*b*
PMMA; 1 vol %	-1.21×10^{10}	−4.51	−0.754	−0.375
PMMA; 10 vol %	-1.21×10^{11}	−4.51	−9.854	−0.399
PS; 1 vol %	-4.27×10^{4}	−2.96	−0.635[a]	−0.249[a]
			-1.51×10^{6} [b]	−2.65[b]
PS; 10 vol %	-4.27×10^{5}	−2.96	-7.97×10^{3} [a]	−1.65[a]
			-5.65×10^{17} [b]	−6.85[b]

[a] Parameters obtained by fitting from 470 to 700 nm [b] Parameters obtained for fitting from 400 to 460 nm.

PMMA and PS composites with 10 vol % solids loading, though the peak intensities in PS composites were weaker than that in the PMMA composites. These absorption peaks indicate that there were absorption losses in these composites. The presence of absorption losses was one of the reasons for the discrepancies between the experimental and theoretical values of *b*, because absorption losses were not accounted for in the theoretical model.

For both PMMA and PS composites, the measured and theoretical values of *A* were also found to be significantly different (see Table 1). As mentioned earlier, factors that would affect the values of *A* include optical path length, "particle size" and solids loading. The discrepancies in the *A* values can be attributed to several possibilities, including actual characteristic lengths of the scattering center, multiple scattering effects, and efficiencies of absorption and refraction which affects the actual optical path length, *x*. Considering the poor dispersion of CeF_3:Yb−Er nanoparticles especially at high solids loadings (see Figures 2 and 3), the characteristic length for the scattering centers (i.e., particle clusters) was larger than that of primary particle size. Different regions within the submicrometer- and micrometer-sized particle clusters (i.e., particle aggregates or agglomerates) would serve as additional scattering centers. These scattering centers would result in interference effects that arise from the interactions of the different scattered light from different parts of the same particle cluster. The effects from these additional scattering centers would be governed mainly by particle morphology and the interparticle (e.g., interparticle distance) and (e.g., fractal shape) intraparticle structures.

4. CONCLUSIONS

Bright infrared-emitting transparent nanocomposites of unmodified CeF_3:Yb−Er nanoparticles with low-cost polymers, PMMA and PS were prepared in this work. In this work, transparent composites with high solids loading were obtained by matching the refractive index of the polymer and inorganic particle without using any complex processing or particle surface modification. PS nanocomposites exhibited better transparency than the PMMA nanocomposites, especially at high solids loading (≥10 vol %). It was found that the optical transparency of PMMA nanocomposites was more significantly affected by the increase in solids loading and inorganic particle size due to the larger refractive index mismatch of the PMMA nanocomposites compared to that of PS nanocomposites. Rayleigh scattering theory was used to provide a theoretical estimate of the scattering losses in the polymer composites. The poor fit between measured and theoretical predictions can be attributed to the inherent inadequacies of the Rayleigh scattering model and lack of consideration for the contribution of absorption losses and multiple scattering effects. The presence of submicrometer- and micrometer-sized particle clusters especially at high solids loading led to additional scattering centers, which gave rise to multiple scattering.

Acknowledgment. We thank V. Starovoytovy of Rutgers University for his assistance with TEM. M.C.T. and R.E.R. acknowledge the Defense Advanced Research Projects Agency (ONR-N00014-08-1-0131) for funding this research. S.D.P. and R.E.R. acknowledge Advanced Technologies and Regenerative Medicine, LLC, a Johnson and Johnson company (006763-001-006), for funding support.

Supporting Information Available: Infrared emission and transmittance spectra of the polymer composites (PDF). This material is available free of charge via the Internet at http://pubs.acs.org.

REFERENCES AND NOTES

(1) Becker, P. C.; Olsson, N. A.; Simpson, J. R. *Erbium-Doped Fiber Amplifiers: Fundamentals and Technology*; Academic Press: San Diego, 1999.
(2) Digonnet, M. J. F. *Rare Earth Doped Fiber Lasers and Amplifiers*; Marcel Dekker: New York, 1993.
(3) Dejneka, M.; Riman, R. E.; Snitzer, E. *J. Am. Ceram. Soc.* **1993**, *76*, 3147–3150.
(4) Ballato, J.; Dejneka, M.; Riman, R. E.; Snitzer, E.; Zhou, W. *J. Mater. Res.* **1996**, *11*, 841–849.
(5) Righini, G. C.; Pelli, S. *J. Sol−Gel Sci. Technol.* **1997**, *9*, 991–997.
(6) McFarlane, R. A.; Lui, M.; Yap, D. *IEEE J. Selected Topics Quantum Electronics* **1995**, *1*, 82–91.
(7) Steckl, A. J.; Heikenfeld, J. C.; Lee, D. S.; Garter, M. J.; Baker, C. C.; Wang, Y.; Jones, R. *IEEE J. Sel. Top. Quantum Electron.* **2002**, *8*, 749–766.
(8) Townsend, P. D. *Vacuum* **1998**, *51*, 301–304.
(9) Slooff, L. H.; de Dood, M. J. A.; van Blaaderen, A.; Polman, A. *Appl. Phys. Lett.* **2000**, *76*, 3682–3684.
(10) Koeppen, C.; Yamada, S.; Jiang, G.; Garito, A. F.; Dalton, L. R. *J. Opt. Soc. Am. B* **1997**, *14*, 155–162.
(11) Polman, A. *Proc. SPIE* **2000**, *3942*, 2–13.
(12) Slooff, L. H.; van Blaaderen, A.; Polman, A.; Hebbink, G. A.; Klink, S. I.; van Veggel, F. C. J. M.; Reinhoudt, D. N.; Hofstraat, J. W. *J. Appl. Phys.* **2002**, *91*, 3955–3980.
(13) Polman, A.; van Veggel, F. C. J. M. *J. Opt. Soc. Am. B* **2004**, *21*, 871–892.
(14) Riman, R. E.; Kumar, G. A.; Banerjee, S.; Brennan, J. G. *J. Am. Ceram. Soc.* **2006**, *89*, 1809–1815.
(15) Binnemans, K. *Chem. Rev.* **2009**, *109*, 4283–4374.
(16) Kumar, G. A.; Chen, C. W.; Riman, R. E.; Chen, S.; Smith, D.; Ballato, J. *Appl. Phys. Lett.* **2005**, *86*, 241105/1–241105/3.
(17) Kumar, G. A.; Chen, C. W.; Ballato, J.; Riman, R. E. *Chem. Mater.* **2007**, *19*, 1523–1528.
(18) Riman, R. E.; Ballato, J. Optically transparent nanocomposite materials, *U.S. Patent 7,094,361*, 2006.
(19) Caseri, W. R. *Mater. Sci. Technol.* **2006**, *22*, 807–817.
(20) Althues, H.; Henle, J.; Kaskel, S. *Chem. Soc. Rev.* **2007**, *36*, 1454–1465.
(21) Lü, C.; Yang, B. *J. Mater. Chem.* **2009**, *19*, 2884–2901.
(22) DiMaio, J. R.; Kokuoz, B.; Ballato, J. *J. Am. Chem. Soc.* **2008**, *130*, 5628–5629.
(23) Boyer, J. C.; Johnson, N. J. J.; van Veggel, F. C. J. M. *Chem. Mater.* **2009**, *21*, 2010–2012.

(24) Chai, R.; Lian, H.; Li, C.; Cheng, Z.; Hou, Z.; Huang, S.; Lin, J. *J. Phys. Chem. C* **2009**, *113*, 8070–8076.
(25) Chai, R.; Lian, H.; Hou, Z.; Zhang, C.; Peng, C.; Lin, J. *J. Phys. Chem. C* **2010**, *114*, 610–616.
(26) Chai, R.; Lian, H.; Cheng, Z.; Zhang, C.; Hou, Z.; Xu, Z.; Lin, J. *J. Colloid Interface Sci.* **2010**, *345*, 262–268.
(27) Hiemenz, P. C.; Rajagopalan, R. *Principles of Colloid and Surface Chemistry*, 3rd ed.; Marcel Dekker: New York, 1997.
(28) Laurin, T. C. *The Photonics Design and Application Handbook 3*, 45th international ed.; Laurin Publishing: Pittsfield, MA, 1999.
(29) Jillavenkatesa, A.; Dapkunas, S. J.; Lum, L-S. H. *Particle Size Characterization*; National Institute of Standards and Technology Speciacl Publication 960-1; U.S. Government Printing Office: Washington, D.C., 2001.
(30) Tan, M. C.; Kumar, G. A.; Riman, R. E. *Opt. Exp.* **2009**, *17*, 15904–15910.
(31) Hass, G.; Ramsey, J. B.; Thun, R. *J. Opt. Soc. A* **1959**, *49*, 116–120.
(32) Wang, Q.; Tan, M. C.; Zhuo, R.; Kumar, G. A.; Riman, R. E. *J. Nanosci. Nanotechnol.* **2010**, *10*, 1685–1692.

AM100228J